

CO Oxidation on Pd(111): A First-Principles-Based Kinetic Monte Carlo Study

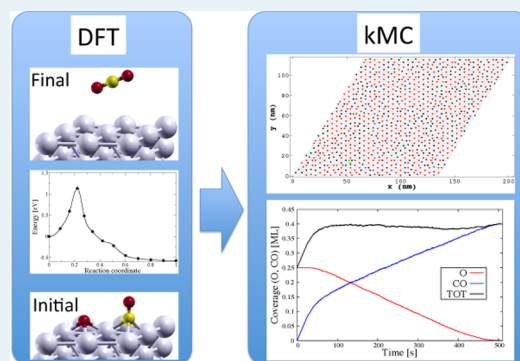
Simone Piccinin^{*,†} and Michail Stamatakis[‡]

[†]CNR-IOM DEMOCRITOS c/o SISSA, Via Bonomea 265, 34136 Trieste, Italy

[‡]Department of Chemical Engineering, University College London, Torrington Place, London WC1E 7JE, United Kingdom

S Supporting Information

ABSTRACT: CO oxidation on O-precovered Pd(111) surfaces exhibits remarkably different reactivities at different temperatures, which correlate with structural changes in the atomic O overlayer. Stoichiometric titration experiments by Nakai et al. (*J. Chem. Phys.* **2006**, *124*, 224712) show that although the $p(2 \times 2)$ ordered phase is inert, the $(\sqrt{3} \times \sqrt{3})$ and $p(2 \times 1)$ phases that form at 320 and 190 K, respectively, have different apparent activation energies and reaction orders with respect to O coverage. In this work, we perform first-principles-based kinetic Monte Carlo (kMC) simulations to understand the behavior of this catalytic system and shed light on the origin of the changes in reactivity. Accounting explicitly for lateral interactions among adsorbates and for their impact on the activation energies of the elementary processes, our simulations reproduce quantitatively the main features of the experimental measurements, and we show that the relative rates of CO adsorption and surface reaction are different as the temperature changes. We find that ordering of the adsorbate layer strongly depends on the strength of the lateral interactions but does not have a significant role on the catalytic properties of the system.



1. INTRODUCTION

Lateral interactions among adsorbates on metal surfaces are known to play an important role in heterogeneous catalysis.¹ They can induce spatial correlations among adsorbates and drive the formation of ordered structures at the surface. Typical examples include the formation of oxygen $p(2 \times 2)$ domains on closed pack surfaces of metals like Ag, Ru, Ni, Pt, and Pd. Lateral interactions also influence the adsorption energy of atoms and molecules, usually leading to a decrease of the adsorption energy at increasing coverages,² and hence have a large role in determining the phase diagram of the adsorbate overlayer on a catalytic surface.³ Affecting the adsorbates' adsorption energy, these interactions not only influence the structural properties of an overlayer but also modify the rates of elementary reactions, because activation energies correlate with adsorption energies through the Brønsted–Evans–Polanyi (BEP) relationship.^{4,5}

In the field of heterogeneous catalysis, an important example of a reaction where lateral interactions play a significant role is CO oxidation on noble metals like Pt and Pd. This reaction proceeds through a Langmuir–Hinshelwood mechanism, in which both reactants are adsorbed on the surface before combining to form CO_2 .^{6,7} In the case of Pt(111), depending on the CO coverage, there is a change of the reaction order with respect to the reactants coverage, which has been interpreted as a change of the reaction site from isolated adsorbates to islands periphery.⁸ In the case of Pd(111), lateral interactions seem to play an even larger role.⁹ Preadsorbed

oxygen, arranged in a $p(2 \times 2)$ ordered phase, compresses into denser $(\sqrt{3} \times \sqrt{3})$ domains upon exposure to a CO atmosphere, to accommodate the adsorption of CO molecules. Depending on temperature and pressure, the oxygen domains are found to transition to a $p(2 \times 1)$ ordered phase or to mixed O + CO areas. The most striking result is the effect these structural rearrangements have on the catalytic properties of the system. Although the initial $p(2 \times 2)$ phase is inert toward CO oxidation, the transition to denser oxygen domains is accompanied by a marked increase in the catalytic activity. In particular, at around 320 K, the appearance of the $(\sqrt{3} \times \sqrt{3})$ phase correlates with an extremely low apparent activation energy of 0.04 ± 0.02 eV. The reaction, in this regime, is found to have approximately order 1/2 with respect to oxygen coverage, albeit at coverages below 0.05 ML. At lower temperatures, around 190 K, the oxygen domains give rise to ordered $p(2 \times 1)$ structures, and the reaction proceeds with an apparent activation energy of 0.29 ± 0.03 eV and exhibits approximately order 1 with respect to oxygen coverage.

Lateral interactions are typically estimated empirically from experimental data (e.g., from temperature programmed desorption) under the assumption of pairwise additivity. Theoretical simulations based on density functional theory (DFT) have also been used to obtain from first-principles, without any

Received: March 21, 2014

Revised: May 14, 2014

Published: May 27, 2014

empirical parameters, accurate descriptions of how adsorbates interact.^{2,10–12} The most general approach, in this respect, is the so-called cluster expansion (CE) or lattice gas Hamiltonian approach.¹³ The energy of any spatial arrangement of adsorbates on a lattice is written as a sum of contributions including on-site formation energies, two-body attractions or repulsions, as well as many-body contributions. Being orthogonal to each other, the “figures” (or “clusters”) included in such an expansion, in the limit of an infinite set, form a complete basis to represent the Hamiltonian of the system. In practice, the sum is truncated to only include figures with up to a specific number of adsorbates whose spatial separation is less than a cutoff; for instance, one may account for up to the fourth nearest-neighbor interactions between three adsorbates at most. It is possible to systematically check for the accuracy of the cluster expansion by increasing the basis set used to represent the Hamiltonian. The interaction parameters are then fitted against a set of DFT calculations, and the CE thus obtained can typically reproduce the DFT energies per adsorbate within a few meV. Clearly, the overall accuracy of the CE depends on the accuracy of the underlying DFT energies, as discussed in refs 11 and 14.

This approach has been widely used in lattice-based Monte Carlo simulations to predict equilibrium properties of adsorbates on metal surfaces, such as the critical temperature of order–disorder phase transitions and the surface phase diagram of simple adsorption systems.^{15–17} The application of the CE approach in kinetic simulations, on the other hand, is still in its infancy. Schneider and co-workers recently investigated the kinetics of NO oxidation on Pt(111) by means of equilibrium Monte Carlo (MC) calculations based on the CE approach.¹⁸ Kinetic properties were then extracted linking adsorption energies to activation energies through the BEP relationship. The most powerful approach for tackling the dynamics of a catalytic system, however, is kinetic Monte Carlo (kMC), where the interplay among elementary reactions is fully accounted for via stochastic simulations. The rates of the elementary steps can be obtained, within the transition state theory framework, from DFT calculations. In this context, the impact of the limited DFT accuracy of activation energies has been discussed in recent reviews.¹⁹ This approach has been used, for example, to model CO oxidation on several metal surfaces, including Pd(100),^{20,21} Pt(100),²² Rh(100),²³ and Pt(111),²⁴ as well as on metal oxide surfaces like RuO₂(110).²⁵ Reviews on kMC studies of CO oxidation as well as a variety of other chemistries have recently appeared.^{14,26} Some of these studies, and in particular the one by Nagasaka et al.,²⁴ include the effects of lateral interactions of the activation energies, modeled assuming a fixed geometry for the transition state and accounting for pair interactions only. In this work, on the other hand, we compute from first-principles the full reaction path at different coverages, extract the BEP correlation between activation energy and reaction energy, and compute the environment-dependent barriers on the basis of a CE whose accuracy has been carefully monitored.¹⁷ Coupling kMC with the CE makes it possible to capture the dependence of the rates of elementary processes on the spatial arrangement of adsorbates.²⁷ Clearly this goes beyond the description afforded by microkinetic models, where such effects are either ignored or treated at the mean field level.²⁸

In this work, we perform kMC simulations of CO oxidation on Pd(111) fully accounting for the effect of lateral interactions with the use of CEs. In our approach, both kinetic parameters

such as the activation energies and the prefactors of elementary reactions, as well as the interactions among adsorbates are derived from DFT calculations, without the use of any parameter determined empirically. We are able to reproduce qualitatively and quantitatively the main experimental features of this catalytic system, and we are able to rationalize the strong dependence of the kinetics on the temperature and pressure conditions. We show that the ordering of the oxygen adsorbates has a negligible influence on the rate of CO oxidation, whereas the main effect of lateral interactions is to influence the activation energy of the elementary reactions, thus leading us to a new interpretation of the experimental findings of Nakai et al.⁹ We discuss also the limitations of our approach and in particular the absence of some of the ordered phases in our simulations.

2. COMPUTATIONAL METHODS

Kinetic Monte Carlo. For our purposes, we use the Graph-Theoretical kinetic Monte Carlo (GT-kMC) framework^{27,29} as implemented in the software package Zacros.³⁰ This framework incorporates a general cluster-expansion approach for capturing lateral interactions, the accurate modeling of which is crucial for our simulations. The input to the latter consists of the operating conditions (temperature, pressure, gas phase composition), a lattice structure that represents the catalytic surface, an energetics model that includes the figures representing adsorbate–adsorbate lateral interactions (single- and multibody contributions), and a reaction mechanism that includes the elementary events (adsorption, desorption, diffusion, reaction) that can occur in our system. In addition, one can optionally provide an initial configuration of the adsorbates on the lattice; in the absence thereof, the simulation is initialized with an empty lattice. The first step in the kMC algorithm is the scanning of the lattice and the identification of all the possible elementary events that can occur, out of the list of events included in the reaction mechanism. The simulator then creates a lattice process queue containing the random occurrence times of these events (more details about how these are calculated follow) and executes the first (most imminent) event in the queue. The simulation time is subsequently updated, along with the lattice state and energetics, to reflect the occurrence of that event. The lattice process queue is also updated, by deleting all processes that involved the entities just removed as reactants, detecting and inserting processes in which the newly added entities (products) can participate, and finally, updating the rates of events in the vicinity of the recent reaction event to account for the new energetic interactions. The whole procedure is repeated by simulating the currently most imminent event, thereby generating a stochastic trajectory that can be postprocessed to yield observables, such as average species coverages, order parameters for the different overlayer phases, and of course, reaction rates.

Lattice Energetics. For the calculation of the energy of the lattice for a given configuration, the cluster expansion approach is used, as implemented in the GT-kMC framework.²⁷ The Hamiltonian is given as

$$H(\sigma) = \sum_{k=1}^{N_c} \frac{ECI_k}{GM_k} \cdot NCE_k(\sigma) \quad (1)$$

where $H(\sigma)$ denotes the Hamiltonian of the system (energy of a microscopic configuration); N_c is the number of figures/clusters specified in the energetic model; ECI_k is the effective cluster interaction of figure k , namely, the contribution of one such figure to the total energy; GM_k is the graph-multiplicity of that figure (similar to a symmetry number, used to avoid overcounting contributions); and finally, NCE_k is the number of occurrences of figure k in the current lattice configuration, obtained by performing a pattern search on the lattice and counting the possible mappings of figure k on the adlayer (for the technical details please refer to ref 27).

Reaction Kinetics. For each of the possible lattice processes, the rate constant is calculated from an Arrhenius expression of the following form:

$$k_{\text{fwd}} = \frac{k_B T}{h} \cdot \frac{Q^\ddagger}{Q_R} \cdot \exp\left(-\frac{E_{\text{fwd}}^\ddagger(\sigma)}{k_B T}\right) \quad (2)$$

where “fwd” denotes the forward step in a reversible event or just an irreversible event; k_{fwd} is the rate constant thereof; k_B and h are Boltzmann’s and Planck’s constants, respectively; T is the temperature; Q^\ddagger and Q_R are the quasi-partition functions of the transition state and the reactants, respectively; and finally, $E_{\text{fwd}}^\ddagger(\sigma)$ is the activation energy at that specific configuration denoted by σ . For a reversible event, the rate of the reverse reaction is

$$k_{\text{rev}} = \frac{k_B T}{h} \cdot \frac{Q^\ddagger}{Q_P} \cdot \exp\left(-\frac{E_{\text{rev}}^\ddagger(\sigma)}{k_B T}\right) \quad (3)$$

where Q_P is the quasi-partition function of the products. Microscopic reversibility imposes restrictions on the activation energies of the forward and reverse steps; in particular, the following condition needs to be satisfied:

$$\Delta E_{\text{rxn}}(\sigma) = H(\sigma') - H(\sigma) + \Delta E_{\text{gas}} \quad (4)$$

where σ and σ' are the initial and final lattice configurations, respectively; ΔE_{gas} the difference in the gas species energies between final and initial configurations; H denotes the cluster expansion Hamiltonian (from eq 1); and finally, ΔE_{rxn} represents the reaction energy defined as

$$\Delta E_{\text{rxn}}(\sigma) = E_{\text{fwd}}^\ddagger(\sigma) - E_{\text{rev}}^\ddagger(\sigma) \quad (5)$$

Thus, the kinetics model is “built” on the foundation of the adsorbate energetics model, thereby ensuring microscopic reversibility and thermodynamic consistency of the simulation. We still need an *Ansatz* for the activation energies:

$$E_{\text{fwd}}^\ddagger(\sigma) = \max(0, \Delta E_{\text{rxn}}(\sigma), E_{\text{fwd},0}^\ddagger + \omega \cdot (\Delta E_{\text{rxn}}(\sigma) - \Delta E_{\text{rxn},0})) \quad (6)$$

$$E_{\text{rev}}^\ddagger(\sigma) = \max(-\Delta E_{\text{rxn}}(\sigma), 0, E_{\text{rev},0}^\ddagger - (1 - \omega) \cdot (\Delta E_{\text{rxn}}(\sigma) - \Delta E_{\text{rxn},0})) \quad (7)$$

where $E_{\text{fwd},0}^\ddagger$ and $E_{\text{rev},0}^\ddagger$ are the activation energies of the forward and reverse step at the zero coverage limit (i.e., when the surface is occupied only by the reacting species), ω is a parameter termed the proximity factor,³¹ and $\Delta E_{\text{rxn},0}$ is the reaction energy at the zero coverage limit, satisfying:

$$E_{\text{rev},0}^\ddagger = E_{\text{fwd},0}^\ddagger - \Delta E_{\text{rxn},0} \quad (8)$$

It is straightforward to verify that equations eqs 6–8 are in line with eq 5.

Once the rate constant has been calculated for an event (adsorption/desorption, diffusion, or reaction), the random time for the occurrence of that event can be generated. Assuming that the current time in the simulation is t , the time increment τ (also known as time of quiescence or interarrival/waiting time) follows the distribution below:^{29,32}

$$p(\tau) = k_{\text{fwd}}(t + \tau) \cdot \exp\left[-\int_0^\tau k_{\text{fwd}}(t + \tau') d\tau'\right] \quad (9)$$

The equation above is generally applicable to the case where the rate constant may be time-dependent, for instance, during temperature programmed desorption/reaction in which the temperature and subsequently the rate constant change in time. To generate a random sample, τ_s , of the above distribution, one has to solve the following nonlinear equation:^{29,33}

$$\int_0^{\tau_s} k_{\text{fwd}}(t + \tau') d\tau' + \ln(1 - u) = 0 \quad (10)$$

where u is a random number drawn from the uniform distribution.

DFT Calculations. To parametrize the aforementioned energetic and kinetic models, we carried out first-principles calculations using density functional theory (DFT). The DFT calculations presented in this work employ the Perdew–Burke–Ernzerhof (PBE) generalized gradient approximation (GGA)³⁴ for the exchange and correlation functional. We use a plane wave ultrasoft-pseudopotentials³⁵ approach as implemented in the Quantum ESPRESSO package.³⁶ Kinetic energy cutoffs used to represent the electron wave function and density are 27 Ry (367.3 eV) and 200 Ry (2721.1 eV), respectively. We adopt a slab geometry, with four metal layers where the bottom two layers are held fixed in bulk positions. A vacuum of around 12 Å ensures negligible coupling between periodic replicas of the slab. The Brillouin-zone integration is performed using equispaced points equivalent to a (12 × 12 × 1) regular mesh in the (1 × 1) surface unit cell, and the Fermi surface is broadened using a smearing parameter of 0.03 Ry (0.41 eV). All the structures are fully relaxed until the forces on all atoms are below 5×10^{-4} a.u. (0.026 eV/Å). The minimum energy paths and the transition states are calculated using the climbing-image nudged elastic band (CI-NEB) approach.³⁷ The normal-mode analysis is performed at the initial and transition states using the finite displacements method, with a displacement of 0.01 Å.

3. RESULTS AND DISCUSSION

3.1. CONSTRUCTION OF THE CLUSTER EXPANSION

In our model for CO oxidation on Pd(111), we consider two types of adsorbates, CO and O, which can occupy two types of sites, fcc and hcp. Figure 1 shows a schematic of the lattice

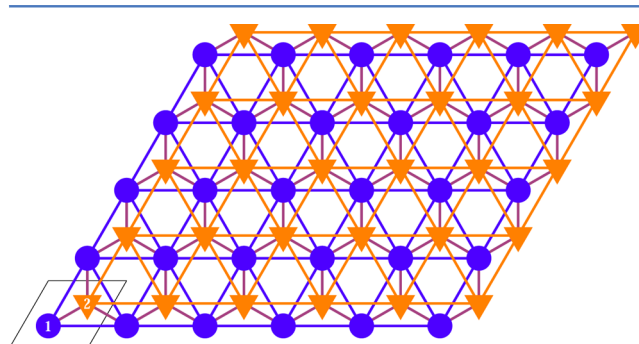


Figure 1. Lattice for the Pd(111) surface used in the kMC simulations. Two kinds of adsorption sites are considered: fcc (1) and hcp (2).

employed in our simulations. In the cluster expansion, in addition to on-site adsorption energies, we consider two-body and three-body lateral interactions among adsorbates. The two-body terms include first, second, and third nearest-neighbor interactions, whereas three-body terms include linear, triangular, and bent figures.¹⁷ The two-body terms comprise O–O, CO–CO, and the mixed term O–CO interactions. The three-body terms comprise 3O, 3CO, 2O–1CO, and 1O–2CO interactions. The interactions among fcc and hcp sites were modeled including only two-body terms. The total number of figures included in our CE is 49. To fit the energetic interactions corresponding to each of these 49 figures, we used a set of 92 DFT calculations, with varying number of O and CO adsorbates in (2 × 2) and (3 × 3) cells. The root-mean-square error between the DFT and CE estimate of the adsorption energy per adsorbate is 9.6 meV, which is in line with similar calculations performed on systems where only one type of adsorbate was considered.⁵ A list of all the figures and

the corresponding interaction energies are reported in the Supporting Information (SI).

3.2. NEB Calculations. To compute the activation energy for CO oxidation, we performed four simulations employing a (3×3) unit cell (see Figure 2 and SI): one in which only the

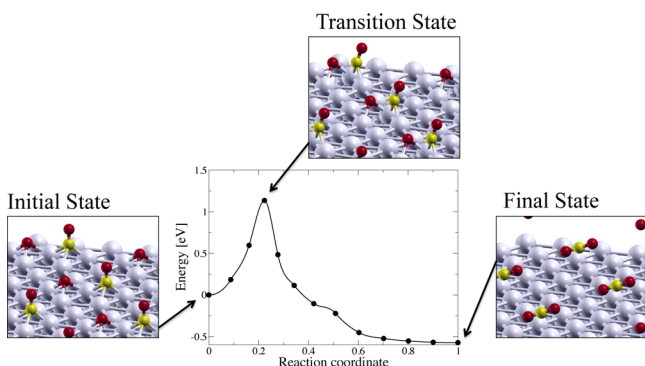


Figure 2. NEB calculation of the minimum energy path for CO oxidation on Pd(111). The figure shows the energy profile along the reaction coordinate and the geometries of initial, transition, and final states in a (3×3) unit cell.

reactants were present and then in the presence of 1, 2, and 4 extra O adsorbates. We then performed simulations using a (2×2) cell and finally a (4×4) cell with 7 O adsorbates, for a total of 6 NEB calculations. In all cases, the reactants are adsorbed on fcc sites, which is the most favorable configuration. Figure 3 shows that there is an approximately linear

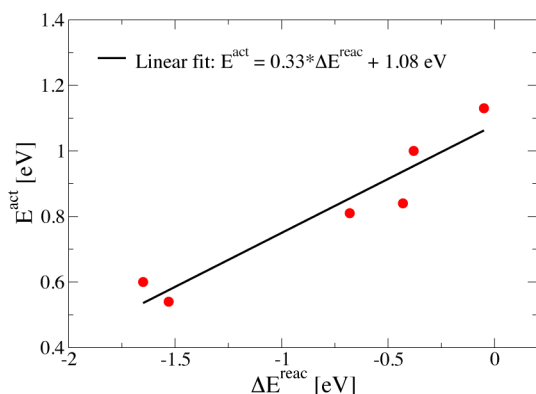


Figure 3. Linear fit of the dependence of the activation energy on the reaction energy.

relationship (Brønsted–Evans–Polanyi (BEP) relationship^{38,39}) between the activation energy E^{act} and the reaction energy ΔE^{react} (i.e., the energy difference between initial and final state). The deviations of around 0.1 eV from perfect linearity are in line with previous estimates reported in the literature.⁴ We then performed a single NEB calculation in which both reactants were adsorbed on HPC sites, and we found the activation energy to be 0.05 eV lower than the corresponding value for the fcc sites. Through these calculations, we estimate the activation energy in the zero coverage limit (E_0^{act}) to be 1.13 and 1.08 eV for the fcc and hcp sites, respectively, which corresponds to the DFT value obtained using the (3×3) unit cell. On the basis of the linear fit presented in Figure 3, a value of $\omega = 0.33$ for the proximity factor (see eq 6) is employed in our kMC simulation to estimate how the effect of lateral interactions on the reaction energy modifies the activation energy.

Similarly, we used the NEB method to compute the activation energies for O and CO diffusion between an fcc and an hcp site, which turn out to be 0.53 and 0.26 eV, respectively. For both events, the proximity factor was set equal to 0.5.

3.3. KMC Simulations. Our kMC simulations aim at understanding the different kinetics observed experimentally as the temperature is lowered from 320 to 190 K. The elementary steps included in our kMC simulations consist of CO adsorption/desorption, CO and O diffusion, and CO oxidation (see Table 1).

Because associative desorption of two O atoms has an energy cost of around 1.9 eV, considerably higher than the barriers of all other elementary steps, molecular O_2 desorption is not considered in our study. To model the “titration” experiment of Nakai et al.,⁹ oxygen is preadsorbed on the Pd(111) surface, at a 0.25 ML coverage. At this coverage, O atoms arrange in an ordered $p(2 \times 2)$ phase. As shown in our previous work,¹⁷ this phase is stable up to around 660 K, where a second-order phase transition to a disordered phase takes place. Thus, the kMC simulation is initialized with a $\text{O}-p(2 \times 2)$ overlayer, which is subsequently exposed to a CO atmosphere at $p(\text{CO}) = 2 \times 10^{-8}$ Torr as in experiments. In our simulations, we took the CO_2 gas molar fraction to be equal to 0, assuming that CO_2 is rapidly removed and does not accumulate in the gas phase. CO_2 dissociation, therefore, cannot take place during the kMC simulation.

Because CO and O diffusion have low barriers and therefore much higher rate constants compared to the other elementary steps, to make the calculation more efficient,¹⁴ we slowed down

Table 1. List of the Elementary Steps Included in the kMC Model^a

step	$A^{\text{fwd}} (\text{s}^{-1})$	$A^{\text{fwd}}/A^{\text{rev}}$	$E_0^{\text{act}} (\text{eV})$	ω
$\text{CO}(\text{g}) + *_{\text{fcc}} \leftrightarrow \text{CO}^*_{\text{fcc}}$	2.55×10^{-3}	2.75×10^{-20}	0	0
$\text{CO}(\text{g}) + *_{\text{hcp}} \leftrightarrow \text{CO}^*_{\text{hcp}}$	2.55×10^{-3}	5.65×10^{-20}	0	0
$\text{CO}^*_{\text{fcc}} \leftrightarrow \text{CO}^*_{\text{hcp}}$	5.28×10^4	1.39	0.26	0.5
$\text{O}^*_{\text{fcc}} \leftrightarrow \text{O}^*_{\text{hcp}}$	7.94×10^8	2.05	0.53	0.5
$\text{CO}^*_{\text{fcc}} + \text{O}^*_{\text{fcc}} \leftrightarrow \text{CO}_2 (\text{g})$	3.27×10^{13}		1.13	0.33
$\text{CO}^*_{\text{hcp}} + \text{O}^*_{\text{hcp}} \leftrightarrow \text{CO}_2 (\text{g})$	1.15×10^{13}		1.08	0.33

^aThe table above includes the prefactor in the forward direction (A^{fwd}) at 320 K; the ratio of the prefactors in the forward and backward directions; the activation energy in the zero-coverage limit (E_0^{act}); and the proximity factor (ω). Prefactors are estimated from transition state theory as outlined in the Supplementary Material of ref 14. We assume non-activated CO adsorption, set the gas molar fraction of CO to 1, and take the effective area of each of the hcp and fcc sites to be 1.5 \AA^2 . For the surface reactions, the prefactors contain only vibrational partition functions, which are calculated using normal mode analysis.

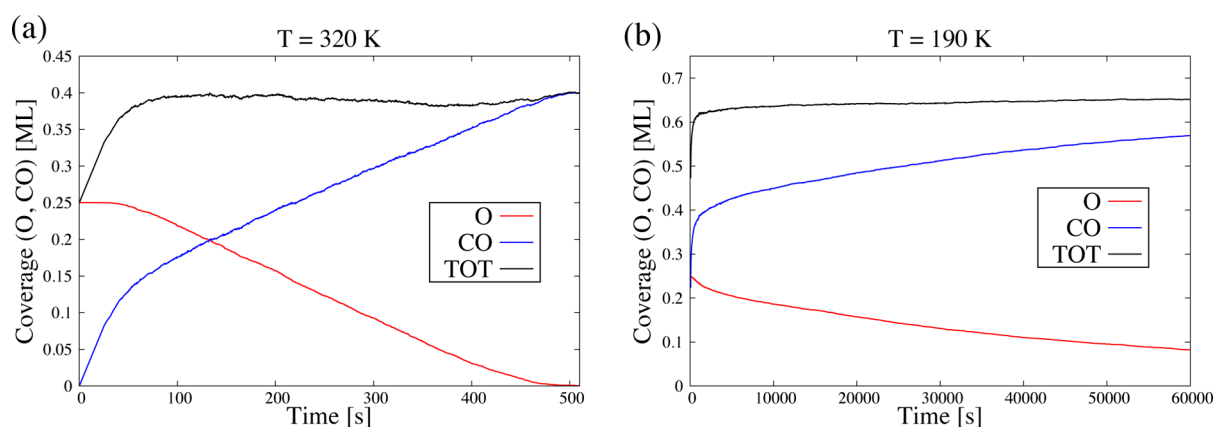


Figure 4. Time evolution of the O and CO coverages at 320 K (a) and 190 K (b). Coverages are normalized with respect to the number of Pd atoms in the (111) surface. The maximum statistical error on coverages, obtained by running 8 kMC simulations, is 14%.

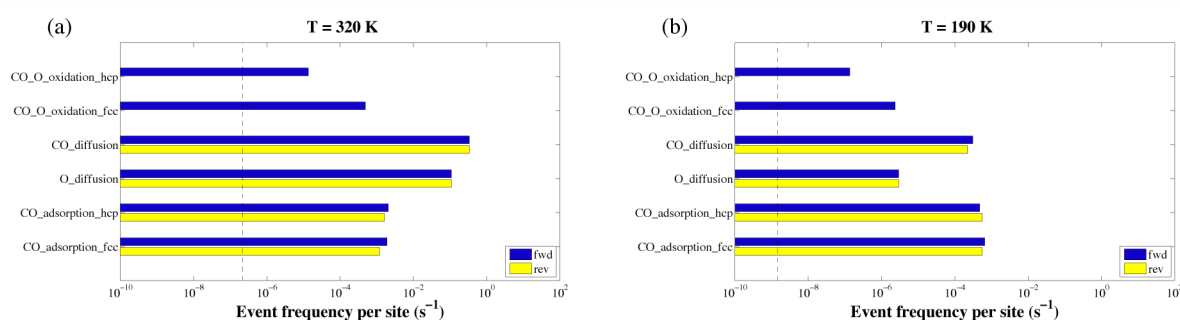


Figure 5. Rates of elementary processes at 320 K (a) and 190 K (b).

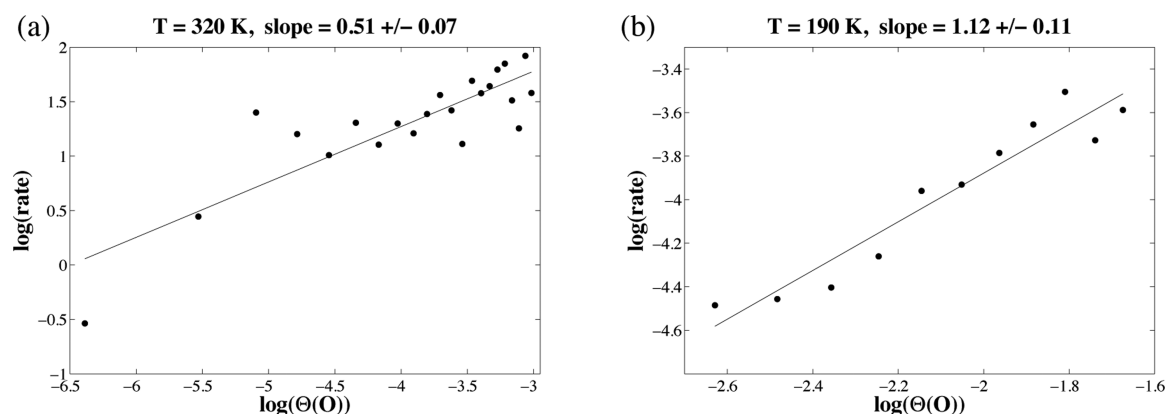


Figure 6. Reaction order with respect to O coverage at 320 K (a) and 190 K (b).

these processes. To achieve this, we reduced the prefactors of O and CO diffusion by 4 and 8 orders of magnitude, respectively. As discussed later, and as shown in the SI, this approximation does not alter significantly the rate of CO oxidation, because diffusion events are still faster than the other elementary processes and are quasi-equilibrated. Additionally, this approach has been mathematically shown to result in negligible (and quantifiable) error in the kMC simulation.⁴⁰

To check the influence of the interaction energies entering the CE on the catalytic properties of the system, we ran several simulations varying the oxygen–oxygen second nearest-neighbor parameter, V_{2nn}^{O-O} . We find that this parameter has a crucial role in the formation of an ordered $p(\sqrt{3} \times \sqrt{3})$ phase. In all simulations presented in the following, unless otherwise stated, we used $V_{2nn}^{O-O} = -0.0050$ eV, rather than the value

obtained from the CE fitting (0.0289 eV). As discussed below, this choice influences the formation of an ordered phase but has no appreciable effect on the kinetics of CO oxidation.

All our kMC simulations, unless stated otherwise, are performed on a 96×96 lattice, using periodic boundary conditions. Figure S2 in the SI provides a comparison of the time evolution of O coverage obtained with various lattice sizes.

3.3.1. T = 320 K. We begin discussing the results of our simulations at 320 K. Consistently with the experiments of Nakai et al.,⁹ we find that there is an induction period (~ 50 s) during which CO is adsorbed on the surface but no CO oxidation takes place (see Figure 4a). During the induction period, the oxygen adsorbates squeeze into higher coverage regions, to accommodate CO adsorbates. The driving force is the large CO adsorption energy (1.93 eV in the zero coverage

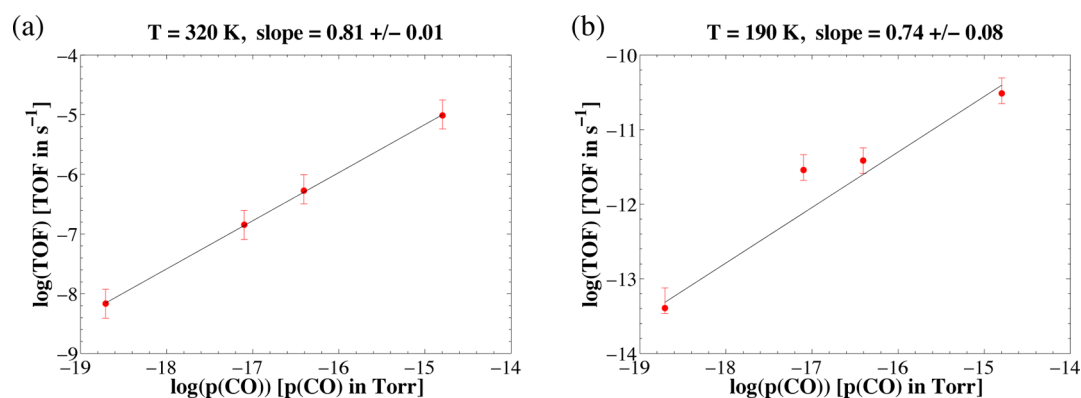


Figure 7. Reaction order with respect to CO pressure at 320 K (a) and 190 K (b).

limit) which compensates for the short-range repulsion among oxygen adsorbates. As soon as the total coverage reaches ~ 0.38 ML, the reaction begins and O is consumed. We find that the reaction is order 0 with respect to the oxygen coverage until the latter approaches very low values (around 0.05 ML), as evidenced by the linear drop in time of the red curve in Figure 4a. During this time, the total O + CO coverage remains approximately constant (black curve), showing that the rate of CO oxidation and the rate at which the CO coverage increases are approximately equal. This is also displayed in Figure 5a, which shows the rates of each elementary step. We can see that the rate of CO adsorption/desorption and the rate of CO oxidation are similar at these conditions. Furthermore, we find that

$$[k_{\text{CO}}^{\text{ads}}(\text{fcc}) - k_{\text{CO}}^{\text{des}}(\text{fcc})] + [k_{\text{CO}}^{\text{ads}}(\text{hcp}) - k_{\text{CO}}^{\text{des}}(\text{hcp})] \approx 2 \times [k^{\text{oxid}}(\text{fcc}) + k^{\text{oxid}}(\text{hcp})] \quad (11)$$

where the factor 2 accounts for the fact that CO oxidation leads to the creation of two empty sites where CO can adsorb. The net result is that an O adsorbate is replaced by a CO adsorbate, and the overall coverage remains approximately constant. Comparing the blue and yellow bars for CO adsorption/desorption in Figure 4a, showing the rates of forward and reverse reaction, respectively, we can also see that this elementary step is not quasi-equilibrated. The partial equilibrium (PE) ratio, defined as $r_{\text{fwd}}/(r_{\text{fwd}} + r_{\text{rev}})$ is equal to 0.61, signaling a sizable departure from quasi-equilibrium (which corresponds to a value of 0.5).

When the oxygen coverage reaches a value of around 0.05 ML, the reaction order of CO oxidation with respect to O coverage becomes approximately 1/2 (see Figure 6a). This is consistent with the results of Nakai et al.,⁹ who reported a reaction order of around 1/2 precisely in that low coverage limit. The reaction order with respect to CO pressure at this temperature is around 0.8 (see Figure 7), again in agreement with the experimental findings (0.8 ± 0.1).

The rate of CO oxidation increases with increasing temperature, with an extremely low apparent activation energy of 0.06 ± 0.04 eV in this temperature range (see Figure 8), in excellent agreement with the experimental value of 0.04 ± 0.02 eV. This very small value has been rationalized by Nakai et al. assuming that the coverage of the reactive CO species, tentatively assigned to CO weakly adsorbed in atop sites, is small. If this is the case, and assuming CO adsorption/desorption to be quasi-equilibrated, the apparent activation energy is simply the difference between the activation energy of the elementary step of CO oxidation and the adsorption

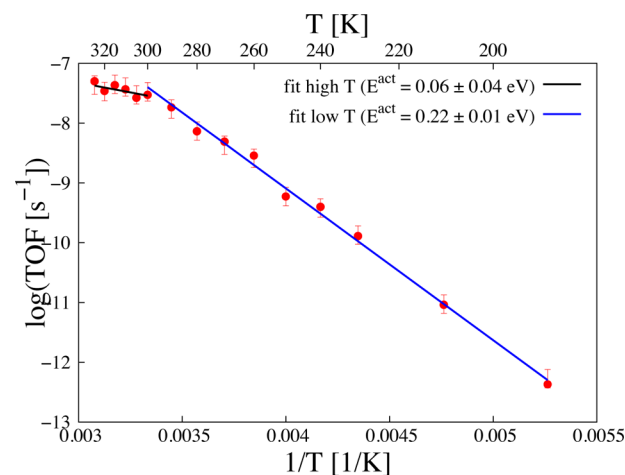


Figure 8. Apparent activation energy in the high-temperature (>300 K, black line) and low-temperature (≤ 300 K, blue line) regimes. These simulations were performed on a 48×48 periodic lattice.

enthalpy of CO, which can therefore be small or even negative.⁴¹

To shed light into the reasons for such a low apparent activation energy, we recorded the intrinsic activation energies of all the CO oxidation events executed during our kMC simulations. The red stems in Figure 9a show the distribution of these activation energies for a simulation at 320 K, whereas the blue histogram shows the distribution of CO oxidation activation energies for all O–CO nearest-neighbor pairs present on the lattice at a particular time ($t = 190$ s), where the O coverage is 0.16 ML and the CO coverage 0.25 ML. Figure 9b shows a similar analysis for the CO adsorption energy. From the overlap of the red stems and the blue histogram, we can see that only loosely bound CO molecules, resulting in lower activation energies, contribute significantly to CO oxidation, whereas those giving rise to higher barriers are rarely selected by the kMC algorithm. Comparing the magnitude of the intrinsic CO oxidation activation energies and of the CO adsorption energy, we can see that the apparent activation energy (0.06 ± 0.04 eV) is not simply given by the difference of these two quantities (0.91 ± 0.06 eV and -1.31 ± 0.14 eV), as in the model advocated by Nakai et al.⁹

In our simulations, however, the apparent activation energy is significantly smaller than the intrinsic activation energies of CO oxidation surface reactions. To show that the dynamics of CO adsorption/desorption indeed influences the value of the apparent activation energy, we stopped the simulation at time

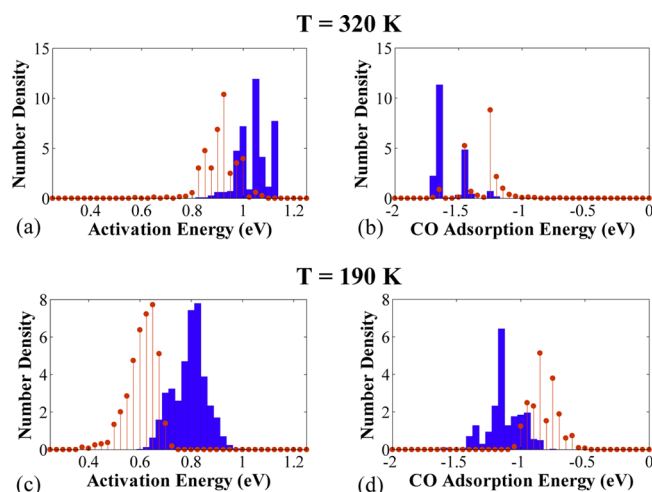


Figure 9. Blue histogram of panel (a) portrays the statistics of the activation energies of the CO oxidation reaction between fcc-bound CO—O pairs encountered on the catalytic surface at $T = 320$ K. These statistics were calculated from a lattice snapshot taken at $t = 194$ s, for which $\Theta(\text{O}_{\text{fcc}})$, $\Theta(\text{CO}_{\text{fcc}}) = 0.10$, $\Theta(\text{O}_{\text{hcp}}) = 0.00022$, $\Theta(\text{CO}_{\text{hcp}}) = 0.13$ ML. The red stem graph, on the other hand, shows the activation energy statistics for the CO oxidation events that actually took place up until that time-point. Therefore, the data presented in the stem graph are essentially weighted by the instantaneous rates of the CO oxidation lattice processes. Panel (b) similarly shows the statistics of the CO adsorption energies of reactive CO—O pairs at $t = 194$ s (blue histogram) and pairs that indeed reacted by that time (red stem plot). Panels (c) and (d) show the corresponding data for $T = 190$ K, for which the snapshot was taken at $t = 1.4 \times 10^4$ s and the coverages were $\Theta(\text{O}_{\text{fcc}}) = 0.16$, $\Theta(\text{CO}_{\text{fcc}}) = 0.22$, $\Theta(\text{O}_{\text{hcp}}) = 0.012$, $\Theta(\text{CO}_{\text{hcp}}) = 0.25$ ML.

$t = 170$ s, switched off both these elementary steps, and then restarted the simulation (see Figure 10). The apparent activation energy at $t > 170$ s becomes 0.85 ± 0.16 eV, in line with the intrinsic activation energy of the CO oxidation elementary step.

In Figure 10, we also notice that right after the switch-off, the rate of O consumption starts dropping and quickly becomes significantly lower compared to $t < 170$ s: the rate of CO oxidation drops from around 5.88 s^{-1} to 0.13 s^{-1} . This happens in spite of the fact that CO is still present at a high coverage on the surface. An identical behavior is found if the switch-off takes

place at $t = 290$ s. This suggests that, beyond a certain coverage threshold, CO is adsorbed on sites where it experiences strong repulsions from the neighboring adsorbates, leading to a smaller adsorption energy and hence a significantly lower activation energy for CO oxidation. When CO adsorption/desorption is stopped, these loosely bound CO molecules quickly react with O, and as soon as they are consumed, the reaction slows down considerably, because the reactants are now the more strongly bound CO molecules.

In fact, inspecting the configuration of neighboring species around the CO and O adsorbate pairs selected by the kMC algorithm to react at $t < 170$ s, we observe that at least one but most often two nearest-neighbor sites are occupied by either O or CO adsorbates (see SI, Figures S9 and S10). Given the significant repulsion experienced by nearest-neighbor pairs, the initial state is strongly destabilized with respect to the zero coverage limit case, leading to a reduction of the activation energy according to eq 6. At $t > 170$ s, after these few pairs in high local coverage environments have reacted, they are unlikely to form again because CO adsorption has been switched off. The activation energy for the CO oxidation is hence higher, and the overall reaction can proceed, but at a much slower rate. Accounting for adsorbate interactions and their impact on the activation energy of the elementary steps is therefore crucial to correctly describe the main features of this catalytic system.

As discussed earlier, at this temperature and pressure, the CO adsorption/desorption reaction is not quasi-equilibrated, questioning one of the key assumptions of the model proposed by Nakai et al.⁹ to explain the low apparent activation energy. Further insights are provided by a simulation in which we artificially increased the prefactors of CO adsorption/desorption by 2 orders of magnitude. In this case, we find the CO adsorption/desorption to be quasi-equilibrated (PE ratio = 0.504), the reaction order with respect to oxygen coverage to be 0.81 ± 0.03 in the whole [0.25 ML, 0.00 ML] range, and the apparent activation energy is now 0.30 ± 0.05 eV (see details in the SI). The catalytic properties of this system are therefore strongly determined not only by the surface reaction but also by the rate of CO uptake from the gas phase.

The zero order with respect to O coverage down to $\Theta(\text{O}) \simeq 0.05$ ML is hence a result of the reaction being limited by both the surface reaction and by the adsorption of CO, because a necessary condition for the reaction to proceed with the rate

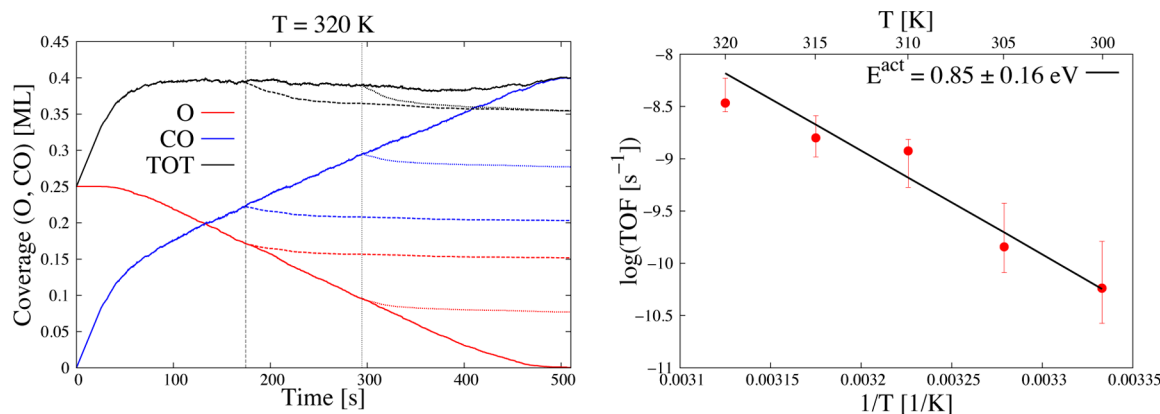


Figure 10. (a) Time evolution of the O and CO coverages at 320 K. Dashed (dotted) lines refer to a simulation where at $t = 170$ s ($t = 290$ s) the CO adsorption/desorption reactions were switched off. (b) Apparent activation energy at $t > 170$ s, after the CO adsorption/desorption reactions were switched off.

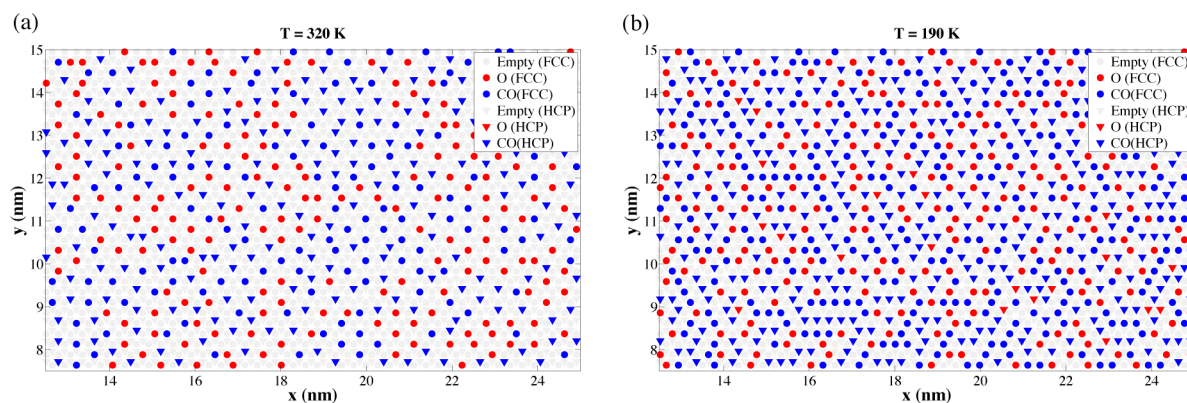


Figure 11. Snapshots of a portion of the lattice during a kMC simulation: (a) after 170 s at 320 K, $\Theta(\text{O}) = 0.17$ ML, $\Theta(\text{CO}) = 0.23$ ML; (b) after 884 s at 190 K, $\Theta(\text{O}) = 0.18$ ML, $\Theta(\text{CO}) = 0.44$ ML.

seen in Figure 4a is for the total coverage to exceed a certain threshold, in this case around 0.38 ML, in order for weakly bound CO adsorbates to form. This explains both the induction period, where CO accumulates on the surface but the barrier for CO oxidation is still high, and the fact that switching off CO adsorption/desorption the reaction quickly slows down before a significant fraction of CO is consumed. We can therefore reconcile this picture with the one proposed by Nakai et al. by identifying CO molecules adsorbed at high (local) coverage as the weakly bound reactive CO species. It is conceivable that, at high coverage, CO might adsorb at atop sites to avoid the strong nearest-neighbor repulsion. While these sites are not included in our model, the qualitative and quantitative agreement of our results with the experimental measurements suggests that a model including hollow sites only is sufficient to capture the salient features of this catalytic system.

In Figure 5, we can see that the diffusion events are quasi-equilibrated and that they are at least 2 orders of magnitude faster than the other elementary processes. Interestingly, we find that CO oxidation takes place mostly among adsorbates on fcc sites, in spite of the fact that the reaction between adsorbates on hcp sites has a lower activation energy. This is because oxygen adsorbs preferentially (by 0.16 eV) in fcc sites. The ratio between occupied fcc and hcp sites is therefore high, making it extremely unlikely to find O and CO on neighboring hcp sites.

An important outcome of our simulations is the effect of the O–O second nearest-neighbor pair interaction parameter ($V_{2\text{nn}}^{\text{O}-\text{O}}$) on the rate of CO oxidation and on the ordering of the O layer. Experiments show that the end of the induction period at 320 K and the start of the CO oxidation correlates with the transition of the O overlayer from a $p(2 \times 2)$ to a $(\sqrt{3} \times \sqrt{3})$ ordered phase. We find that the appearance of the $(\sqrt{3} \times \sqrt{3})$ phase is related to the value of $V_{2\text{nn}}^{\text{O}-\text{O}}$: the value obtained from the fitting of the CE against the DFT data (0.0289 eV) does not lead to the formation of this phase, although slightly lowering this repulsive term (to 0.0200 eV and below), we recover the experimental findings (see Figure S7a,b). Further lowering this value has the effect of increasing the lifetime of the $(\sqrt{3} \times \sqrt{3})$ phase. Remarkably, however, we find that the rate of CO oxidation does not depend on the strength of the $V_{2\text{nn}}^{\text{O}-\text{O}}$ term (see Figure S7c). Ordered and disordered phases, resulting from the lowest and highest values on $V_{2\text{nn}}^{\text{O}-\text{O}}$, respectively, have nearly identical CO oxidation rates. Consistent with the experimental findings, during the induction period, while CO is adsorbed, the O $p(2 \times 2)$ phase squeezes

into a higher coverage phase; however, our simulations suggest that whether the resulting phase is ordered or not does not have any appreciable effects on the catalytic properties of the system.

Figure 11a shows a snapshot of a portion of the lattice after 170 s, corresponding to $\Theta(\text{O}) = 0.17$ ML and $\Theta(\text{CO}) = 0.23$ ML. We see no signs of formation of islands (i.e., there is no segregation of O and CO). We can see, on the other hand, the formation of a homogeneous disordered mixed O+CO phase.

3.3.2. $T = 190$ K. The time evolution of the O and CO coverages at 190 K is shown in Figure 4b. In agreement with the experiments of Nakai et al., we do not find in this case any induction period, and the reaction is approximately order 1 in the O coverage (see Figure 6b). An inspection of the rates of the elementary processes in Figure 5b reveals that in this case, contrary to what happens at 320 K, CO adsorption is much faster than CO oxidation. The surface is therefore quickly saturated with CO, and the reaction is limited by the CO oxidation step, which takes place uniformly over the whole surface. In spite of being quasi-equilibrated, O diffusion is in this case considerably slower than CO oxidation, hence we checked the effect our empirical scaling of the prefactor for this step. Increasing the prefactor for O diffusion by 2 orders of magnitude led to no appreciable difference in the time evolution of the O coverage (see Supporting Information).

The statistical analysis presented in Figure 9 shows that the average activation energy of the CO oxidation surface reaction is 0.61 ± 0.06 eV, and the adsorption energy of the CO molecules participating in the reaction is -0.82 ± 0.10 eV. The lower CO adsorption energy compared to the 320 K case (-1.31 ± 0.14 eV) is a consequence of the repulsive lateral interactions among adsorbates. Because at lower temperature the surface coverage is higher (see Figure 4), this results in a destabilization of CO adsorbates and hence in a lower activation energy for the CO oxidation elementary step compared to the 320 K simulation.

Similar to the high-temperature case, here we find an Arrhenius dependence of the CO oxidation rate, with an apparent activation energy of 0.22 ± 0.01 eV (see Figure 8), which compares well with the experimental value of 0.29 ± 0.03 eV. Interestingly, at this lower temperature (190 K), the system exhibits a higher apparent activation energy, in spite of the fact that the activation energy for the surface reaction is significantly lower. This is due to the increase of the rate of CO adsorption/desorption relative to the rate of CO oxidation on fcc sites, as can be seen comparing panels (a) and (b) in Figure 5.

As soon as CO starts adsorbing, the O $p(2 \times 2)$ ordered phase squeezes into disordered higher coverage areas. At variance with the experiments of Nakai et al., we see no signature of the formation of an ordered $p(2 \times 1)$ phase. As discussed for the 320 K simulations, this might be due to uncertainties in the CE interaction parameters, but our simulations suggest that the presence or absence of long-range order in the O domains has no sizable effects on the rate of CO oxidation.

Figure 11b shows a snapshot of a portion of the lattice, corresponding to $\Theta(\text{O}) = 0.18$ ML and $\Theta(\text{CO}) = 0.44$ ML. As in the high-temperature case, at 190 K as well, we see no segregation of the reactants in O and CO islands but rather the formation of a disordered mixed phase. This is consistent with the order of the reaction being 1 with respect to the oxygen coverage, which can be interpreted as a signature of the reaction proceeding uniformly over the entire lattice and not at the perimeter of islands.⁹

Looking at Figure 8, we can see that the transition between the low- and high-activation-energy regimes takes place around $T \sim 300$ K, a somewhat larger value than what Nakai et al. observed experimentally (~ 220 K). In light of the discussion presented earlier on the effect of the prefactors for CO adsorption/desorption, a possible explanation for this discrepancy is an overestimation of the rate of CO adsorption/desorption.

4. CONCLUSIONS

In this work, we built a first-principles-based kMC model of CO oxidation on O-precovered Pd(111). The accuracy of our approach is such that our simulations reproduce quantitatively the mean features of earlier experiments performed on the same system. Crucially, we were able to rationalize the change in reaction order with respect to O coverage and the change in apparent activation energy seen in experiments as the temperature is lowered from 320 to 190 K. We have shown that a subtle interplay between the rates of CO adsorption/desorption and surface reaction is responsible for the changes in reactivity. At higher temperature, in particular, the order of the reaction with respect to O coverage is zero down to very low coverages. In this regime, as soon as weakly bound CO adsorbates form, they quickly react with O adsorbates to give CO_2 . Analyzing the kMC trajectories, we have shown that the low apparent activation energy is not just the difference between the intrinsic activation energy of the surface reaction and the CO adsorption energy, as a simple model based on the assumption of CO adsorption/desorption being quasi-equilibrated would suggest. This assumption does not hold, and both the apparent activation energy and the reaction order are influenced by the rate of CO adsorption/desorption. Lateral interactions have a strong influence on the CO adsorption energy and hence on the catalytic activity of the system: accounting for their effects allows us to get quantitative agreement with experimental measurements. By altering the O–O lateral interactions, we were able to test the relevance of the formation of ordered structures in the O overlayer. Our simulations show that the presence or absence of ordered phases in the O overlayer is not a key factor in determining the catalytic properties of this system.

■ ASSOCIATED CONTENT

Supporting Information

In the Supporting Information we provide: (i) prefactors for the simulations at 190 K; (ii) the expressions for the order parameters; (iii) tests of the influence of several parameters of the calculations (lattice size, stiffness coefficients) on the catalytic properties of the system; (iv) the time evolution of the activation energies and CO adsorption energy; (v) an explicit description of all the figures included in the cluster expansion. This material is available free of charge via the Internet at <http://pubs.acs.org>.

■ AUTHOR INFORMATION

Corresponding Author

*E-mail: piccinin@iom.cnr.it.

Notes

The authors declare no competing financial interest.

■ ACKNOWLEDGMENTS

The CNR Short Term Mobility Program is acknowledged for partial financial support.

■ REFERENCES

- (1) Kang, H. C.; Weinberg, W. H. *Chem. Rev.* **1995**, *95*, 667–676.
- (2) Li, W.-X.; Stampfl, C.; Scheffler, M. *Phys. Rev. B* **2002**, *65*, 075407.
- (3) Li, W.-X.; Stampfl, C.; Scheffler, M. *Phys. Rev. B* **2003**, *68*, 165412.
- (4) Bligaard, T.; Nørskov, J.; Dahl, S.; Matthiesen, J.; Christensen, C.; Sehested, J. *J. Catal.* **2004**, *224*, 206–217.
- (5) Wu, C.; Schmidt, D.; Wolverton, C.; Schneider, W. *J. Catal.* **2012**, *286*, 88–94.
- (6) Engel, T.; Ertl, G. *J. Chem. Phys.* **1978**, *69*, 1267–1281.
- (7) Campbell, C. T.; Ertl, G.; Kuipers, H.; Segner, J. *J. Chem. Phys.* **1980**, *73*, 5862–5873.
- (8) Nakai, I.; Kondoh, H.; Amemiya, K.; Nagasaka, M.; Shimada, T.; Yokota, R.; Nambu, A.; Ohta, T. *J. Chem. Phys.* **2005**, *122*, 134709.
- (9) Nakai, I.; Kondoh, H.; Shimada, T.; Resta, A.; Andersen, J.; Ohta, T. *J. Chem. Phys.* **2006**, *124*, 224712.
- (10) Tang, H.; Van der Ven, A.; Trout, B. *Phys. Rev. B* **2004**, *70*, 1–10.
- (11) Zhang, Y.; Blum, V.; Reuter, K. *Phys. Rev. B* **2007**, *75*, 1–14.
- (12) Getman, R. B.; Xu, Y.; Schneider, W. F. *J. Phys. Chem. C* **2008**, *112*, 9559–9572.
- (13) Sanchez, J. M.; Ducastelle, F.; Gratias, D. *Physica A* **1984**, *128*, 334–350.
- (14) Stamatakis, M.; Vlachos, D. G. *ACS Catal.* **2012**, *2*, 2648–2663.
- (15) Stampfl, C. *Phase Transitions* **2007**, *80*, 311–332.
- (16) Lazo, C.; Keil, F. J. *Phys. Rev. B* **2009**, *79*, 245418.
- (17) Piccinin, S.; Stampfl, C. *Phys. Rev. B* **2010**, *81*, 155427.
- (18) Wu, C.; Schmidt, D.; Wolverton, C.; Schneider, W. *J. Catal.* **2012**, *286*, 88–94.
- (19) Reuter, K. In *Modeling and Simulation of Heterogeneous Catalytic Reactions*; Deutschmann, O., Ed.; Wiley-VCH Verlag GmbH and Co. KGaA: Weinheim, Germany, 2011; pp 71–111.
- (20) Liu, D.-J.; Evans, J. W. *J. Chem. Phys.* **2006**, *124*, 154705.
- (21) Rogal, J.; Reuter, K.; Scheffler, M. *Phys. Rev. B* **2008**, *77*, 1–12.
- (22) Völkening, S.; Winterlin, J. *J. Chem. Phys.* **2001**, *114*, 6382.
- (23) Liu, D.-J. *J. Phys. Chem. C* **2007**, *111*, 14698–14706.
- (24) Nagasaka, M.; Kondoh, H.; Nakai, I.; Ohta, T. *J. Chem. Phys.* **2007**, *126*, 044704.
- (25) Reuter, K.; Scheffler, M. *Phys. Rev. B* **2006**, *73*, 1–17.
- (26) Liu, D.-J.; Evans, J. W. *Prog. Surf. Sci.* **2013**, *88*, 393–521.
- (27) Nielsen, J.; d’Avezac, M.; Hetherington, J.; Stamatakis, M. *J. Chem. Phys.* **2013**, *139*, 224706.
- (28) Hellman, A.; Honkala, K. *J. Chem. Phys.* **2007**, *127*, 194704.

- (29) Stamatakis, M.; Vlachos, D. G. *J. Chem. Phys.* **2011**, *134*, 214115.
- (30) Stamatakis, M. *Zacros: Advanced Lattice-KMC simulation Made Easy*. http://www.e-lucid.com/i/software/material_modelling/Zacros.html.
- (31) Grabow, L. C.; Gokhale, A. A.; Evans, S. T.; Dumesic, J. A.; Mavrikakis, M. *J. Phys. Chem. C* **2008**, *112*, 4608–4617.
- (32) Gillespie, D. T. *Markov Processes: An Introduction for Physical Scientists*; Academic Press: London, 1992.
- (33) Jansen, A. P. *J. Comput. Phys. Commun.* **1995**, *86*, 1–12.
- (34) Perdew, J. P.; Burke, K.; Ernzerhof, M. *Phys. Rev. Lett.* **1996**, *77*, 3865.
- (35) Vanderbilt, D. *Phys. Rev. B* **1990**, *41*, 7892.
- (36) Giannozzi, P.; Baroni, S.; Bonini, N.; Calandra, M.; Car, R.; Cavazzoni, C.; Ceresoli, D.; Chiarotti, G. L.; Cococcioni, M.; Dabo, I.; Corso, A. D.; de Gironcoli, S.; Fabris, S.; Fratesi, G.; Gebauer, R.; Gerstmann, U.; Gougoussis, C.; Kokalj, A.; Lazzeri, M.; Martin-Samos, L.; Marzari, N.; Mauri, F.; Mazzarello, R.; Paolini, S.; Pasquarello, A.; Paulatto, L.; Sbraccia, C.; Scandolo, S.; Sclauzero, G.; Seitsonen, A. P.; Smogunov, A.; Umari, P.; Wentzcovitch, R. M. *J. Phys.: Cond. Matt.* **2009**, *21*, 395502.
- (37) Henkelman, G.; Uberuaga, B. P.; Johnson, H. *J. Chem. Phys.* **2000**, *113*, 9901.
- (38) Brønsted, N. *Chem. Rev.* **1928**, *5*, 231.
- (39) Evans, M. G.; Polanyi, N. P. *Trans. Faraday Soc.* **1938**, *34*, 11.
- (40) Stamatakis, M.; Vlachos, D. G. *Comput. Chem. Eng.* **2012**, *35*, 2602–2610.
- (41) Elliott, A. J.; Hadden, R. A.; Tabatabaei, T.; Waugh, K. C.; Zemicael, F. Z. *J. Catal.* **1995**, *157*, 153–161.